Accepted for publication in November 10, 2002 edition of the Astrophysical Journal
Preprint typeset using LaTeX style emulateapj v. 19/02/01

EXTREME ULTRAVIOLET ABSORPTION LINES IN Lyα FOREST ABSORBERS AND THE OXYGEN ABUNDANCE IN THE INTERGALACTIC MEDIUM

Randal C. Telfer[1], Gerard A. Kriss[1,2], Wei Zheng[1], Arthur F. Davidsen[1,3], David Tytler[4,5]

Accepted for publication in November 10, 2002 edition of the Astrophysical Journal

ABSTRACT

We create stacked composite absorption spectra from *Hubble Space Telescope* Faint Object Spectrograph data from four quasi-stellar objects to search for absorption lines in the extreme ultraviolet wavelength region associated with Lyα forest absorbers in the redshift range $1.6 < z < 2.9$. We successfully detect O V $\lambda630$ in Lyα absorbers throughout the 10^{13} to $10^{16.2}$ cm^{-2} column density range. For a sample of absorbers with $10^{13.2} < N(\mathrm{H\,I}) < 10^{14.2}$ cm^{-2}, corresponding to gas densities ranging from around the universal mean to overdensities of a few, we measure an O V $\lambda630$ equivalent width of 10.9 ± 3.7 mÅ. We estimate the detection is real with at least 99% confidence. We only detect O IV $\lambda788$, O IV $\lambda554$, O III $\lambda833$, and He I $\lambda584$ in absorbers with Lyα equivalent widths $\gtrsim 0.6$ Å, which are likely associated with traditional metal-line systems. We find no evidence in any subsamples for absorption from N IV $\lambda765$, Ne V $\lambda568$, Ne VI $\lambda559$, Ne VIII $\lambda\lambda770$, 780, or Mg X $\lambda\lambda610$, 625. The measured equivalent widths of O V suggest values of $\langle$O V/H I$\rangle$ in the range -1.7 to -0.6 for $10^{13.2} < N(\mathrm{H\,I}) \lesssim 10^{15}$ cm^{-2}. The lack of detectable O IV absorption except in the strongest absorption systems suggests a hard ionizing background similar to the standard Haardt & Madau spectrum. Using photoionization models, we estimate that the oxygen abundance in the intergalactic medium with respect to the solar value is [O/H] ≈ -2.2 to -1.3. Comparing to studies of C IV, we estimate [O/C] ≈ 0.3 to 1.2. The overabundance of oxygen relative to carbon agrees with other low-metallicity abundance measurements and suggests enrichment of the intergalactic medium by Type II supernovae.

Subject headings: galaxies: intergalactic medium — quasars: absorption lines — ultraviolet: galaxies

1. INTRODUCTION

Early studies of the intergalactic medium (IGM) identified two separate groups of absorbers (e.g., Sargent et al. 1980): (1) "metal-line systems" which have observable metal lines and the strongest Lyα absorption, typically with a Lyα rest-frame equivalent width $\gtrsim 1$ Å, and (2) weaker absorbers having no observable metal lines and comprising what is generally thought of as the "Lyα forest". However, it was suspected that this distinction was due at least partly to observational limitations in the observability of weak metal lines (Tytler 1987), a suspicion that has been verified as technological and computational advances have allowed astronomers to detect metal absorption to much lower column densities. Constraining the abundances of metal ions in the IGM has become an active area of research, since this information can in principle be used to determine the chemical abundances in the IGM as well as shape and strength of the typical metagalactic ionizing background radiation from stars and quasi-stellar objects (QSOs). Of particular interest is the low column density regime ($N(\mathrm{H\,I}) \lesssim 10^{14.5}$ cm^{-2}), since these systems are presumably far away from local sources of metals and ionizing photons and thus offer the best insights into enrichment mechanisms and the ionizing background.

The production of composite or stacked absorption spectra of many Lyα absorbers is an obvious way to increase observational sensitivity. Norris, Peterson, & Hartwick (1983) used the composite technique to claim a detection of O VI $\lambda\lambda1032$, 1038 absorption. The reality of this detection was challenged in a similar study by Williger et al. (1989), but O VI in the IGM was detected unambiguously by Lu & Savage (1993) by creating a composite absorption spectrum of C IV absorbers. Composite spectra were used to detect C IV absorption in systems with $N(\mathrm{H\,I}) \gtrsim 10^{14}$ cm^{-2} at high redshift ($z > 1.7$) by Lu (1991), but Tytler & Fan (1994) failed to detect C IV associated with weaker lines. In a study similar to Lu (1991) but at $z < 0.8$, Barlow & Tytler (1998) found an order of magnitude stronger C IV absorption than Lu (1991).

A more precise way to increase sensitivity is to build bigger telescopes and better instruments in order to acquire higher signal-to-noise ratio (S/N), higher resolution data. With the HIRES instrument on the 10m Keck I telescope, individual C IV features can be detected down to a column density of $N(\mathrm{C\,IV}) \sim 10^{12}$ cm^{-2}. The majority of Lyα absorbers with $N(\mathrm{H\,I}) > 3 \times 10^{14}$ cm^{-2} exhibit such absorption (Tytler et al. 1995; Cowie et al. 1995; Songaila & Cowie 1996). Besides allowing for the direct detection of weaker lines, the existence of such high quality data has opened the door to an additional detection method introduced by Cowie & Songaila (1998), that of comparing the individual pixel optical depths of Lyα to the expected position of corresponding metal lines. Cowie & Songaila (1998) and Ellison et al. (2000) use this technique to detect

[1] Center for Astrophysical Sciences, Johns Hopkins University, Baltimore, MD, 21218-2686
[2] Space Telescope Science Institute, 3700 San Martin Drive, Baltimore, MD, 21218
[3] Deceased 2001 July 19
[4] Center for Astrophysics and Space Science, University of California, San Diego, La Jolla, CA, 92093-0424
[5] Visiting Astronomer, W. M. Keck Observatory, which is a joint facility of the University of California, the California Institute of Technology, and NASA

C IV absorption down to an H I optical depth of $\tau_{\rm HI} \lesssim 1$. Schaye et al. (2000) have used the optical depth technique to detect O VI to optical depths down to $\tau_{\rm HI} \sim 0.1$.

Studies have concentrated on C IV not only due to the fact that it is expected to be one of the strongest features associated with the IGM (Rauch, Haehnelt, & Steinmetz 1997; Hellsten et al. 1998), but also largely because of its near ideal location in wavelength space. With a wavelength of 1549 Å, this absorption feature is near enough to Lyα λ1216 that both features can easily be acquired with the same observations, but far enough above Lyα that the feature will be longward of the Lyα forest for a significant span in redshift. Although C IV is a good tracer of metals in the IGM, in standard photoionization models the O VI $\lambda\lambda$1032, 1038 Å doublet is expected to be a stronger feature at H I column densities $\lesssim 10^{15}$ cm^{-2} (Hellsten et al. 1998). Unfortunately, although the wavelength of C IV makes it very appealing for absorption studies, the O VI $\lambda\lambda$1032, 1038 Å doublet could hardly reside in a worse portion of the spectrum. The region of O VI absorption is muddled not only by Lyα absorption but by higher order Lyman lines as well, making detections much more difficult. Fortunately, Schaye et al. (2000) have overcome this difficulty to detect O VI in the diffuse IGM, although they make no quantitative claims as to the implied amount of O VI in the IGM.

The extreme ultraviolet (EUV) absorption region has been largely ignored, not because this region contains no useful information, but because the best available data in this region, that from the *Hubble Space Telescope* (*HST*) Faint Object Spectrograph (FOS), is inferior in resolution and S/N to that used at longer wavelengths. However, some of the strongest expected absorption features occur in this region, in particular O V λ630 and O IV λ788 (Verner, Tytler, & Barthel 1994). The O V feature is especially worthy of interest because its large oscillator strength ($f = 0.514$, greater than H I Lyα) should make it competitive in strength to the O VI feature even at column densities down to $\sim 10^{13}$ cm^{-2}. Despite the fact that the FOS has rather low resolution by modern standards ($R \approx 1300$), searching for O V rather than O VI has the advantage that the features are in a spectral region where the Lyα forest is less dense owing to the strong evolution of the density of lines with redshift. The detection of oxygen lines in the IGM can be used to infer the oxygen abundance, which is expected to be overabundant relative to carbon with respect to the solar ratio if the early universe is enriched by Type II supernovae. Strong evidence for such abundance patterns are seen at high redshift in Lyman-limit systems (Reimers et al. 1992; Köhler et al. 1999), damped Lyα absorbers (Pettini, Lipman, & Hunstead 1995; Lu et al. 1996), and C IV absorbers (Davé et al. 1998; Songaila 1998). Here we extend this work to the lower column density regime by carrying out a statistical search for absorption in the EUV using the presently available data.

In §2 we discuss the data and the spectral selection criteria that we use for this study. We begin §3 by discussing the characterization of our Lyα absorber sample from optical data. This is followed by a presentation of the details of the technique that we use to generate the stacked absorption spectra and the method for measuring the equivalent width of the resulting absorption features. In §4 we describe the results of our search for various samples selected by the strength of Lyα absorption, particularly the detections of O V. We consider the implications of our results in §5 by comparing the measurements and limits on the equivalent widths of the absorption features to simulated data to constrain the abundance ratios of the relevant ions to H I. Using photoionization models, we then infer the abundance of oxygen in IGM. We provide a brief summary of our results in §6.

2. DATA

We have searched the *HST* archives for QSO spectra suitable for detecting EUV absorption features in the Lyα forest, with the primary goal being the detection of O V λ630. To include an object in this study, we require that:

1. Data are available shortward of 630 Å in the QSO emission frame, making the O V feature accessible.
2. The data are obtained with the FOS high-resolution gratings.
3. The S/N in the region of the O V absorption is high enough that the rms deviation of the pixels is dominated by absorption features rather than Poisson noise. For the typical density of lines in the applicable redshift range ($1.6 < z < 2.9$), the necessary S/N is ~ 5 per pixel. At this S/N, we can make a fairly reliable determination of the continuum level, which is necessary for our study.
4. We have access to high-quality optical spectra for determining the redshift and strength of the Lyα forest lines.

We have found four QSOs that match these criteria. The FOS data for these QSOs were reduced in 2001 July with the best available reference files. In Table 1 we list these objects, their redshifts, the total exposure time of the FOS data with each grating, and the dates the data were obtained. The zero-point shift for the wavelength scale given in of the last column will be discussed in §3.3. All of the data were obtained with the red Digicon detector on the FOS. A G190H spectrum of HS 1700+6416 was obtained with the blue Digicon on 1997 May 29. However, the data are of somewhat lower resolution and for consistency we use only the data from the red Digicon.

For all four objects we have access to Keck HIRES spectra for examining the H I Lyα forest. The spectrum for HE 2347–4342 is courtesy of A. Songaila and is discussed in Songaila (1998). Two of the other three spectra are discussed elsewhere, and we point the reader to the corresponding articles for details: Köhler et al. (1999) for HS 1103+6416 (1997 April 9 data only) and de la Varga et al. (2000) for HE 1122–1649. The spectrum of HS 1700+6416 consists of a 4300 second exposure on 1995 May 10. This spectrum covers wavelengths from 3727 Å to 5523 Å with a typical S/N of ~ 50 per resolution element.

3. ANALYSIS

3.1. *Lyα Forest Data*

The Keck HIRES data are normalized to the continuum by fitting a spline by hand, placing nodes at what appear to be unabsorbed portions of the spectra. We then fit

TABLE 1
FOS DATA

Object	z	Grating	Exposure (s)	Date	Shift (Å)
HS 1103+6416	2.190	G270H	5336	1996 Oct 31	+0.10
		G190H	8628	1996 Oct 31	+0.59
HE 1122–1649	2.400	G270H	780	1996 Jul 18	+0.30
		G190H	5620	1996 Jul 18	+1.25
HS 1700+6416	2.743	G270H	9000	1992 Dec 13	0.00
		G190H	16120	1992 Dec 12–13	+0.85
HE 2347–4342	2.885	G270H	1320	1996 Jun 7	+0.80
		G190H	7930	1996 Jun 7	+1.05

the spectra in sections of ~ 50 Å down to the redshifted position of Lyβ. We use the IRAF task *specfit* to fit the individual absorption features with Gaussians in optical depth:

$$\tau = \tau_0 \ \exp\left[-\left(\frac{\lambda-\lambda_0}{\lambda_0 b/c}\right)^2\right]. \quad (1)$$

Each absorption feature is thus described by three free parameters: the central wavelength λ_0, the optical depth at line center τ_0, and the Doppler width b. In a few cases where the blending is severe, the b-parameter is fixed at 30 km s^{-1}, a typical value for Lyα forest lines (Rauch et al. 1992; Hu et al. 1995), to prevent b from taking on an unreasonable value. We fit all lines with peak optical depths $\gtrsim 0.1$, although lines weaker than this were sometimes fit to deblend stronger lines.

We impose several selection criteria on our list of Lyα forest lines:

1. As is frequently done in Lyα forest studies, we ignore lines shortward of Lyβ in the rest frame of the QSO to avoid confusion of Lyα lines with higher-order lines.

2. We discard lines within 5000 km s^{-1} of the QSO rest frame in order to avoid contamination from the proximity effect (see e.g. Scott et al. 2000). This should also eliminate many associated absorbers, which often occur near the QSO in velocity space. However, some known associated absorbers are displaced substantially more than 5000 km s^{-1} blueward of the QSO redshift (Jannuzi et al. 1996; Hamann, Barlow, & Junkkarinen 1997). We assume that such systems are rare and not a significant source of contamination in our sample.

3. We do not use lines that correspond to known Lyman-limit systems. These high-column-density systems have been well-studied on an individual basis (Vogel & Reimers 1995). Since we have data at the Lyman limit for all candidate lines by virtue of our choice of sample, it is easy to identify Lyman limit features with $\tau \gtrsim 0.1$, corresponding to H I column densities $\gtrsim 10^{16.2}$ cm^{-2}.

4. We eliminate lines that are identified as likely metal lines associated with Lyman-limit or metal-line absorption systems.

5. We ignore features in wavelength regions that are contaminated by strong clusters of such metal lines.

6. We dismiss lines with $b < 14$ km s^{-1} as probable unidentified metal lines. Detailed studies of the distribution of b (Hu et al. 1995; Kirkman & Tytler 1997) show that there is a sharp cutoff at around 20 km s^{-1} and virtually no lines with $b < 14$ km s^{-1}.

7. We also exclude lines with $b > 80$ km s^{-1}. Although a few of these lines are probably real, they are certainly atypical. Some are likely due to blending.

It is straightforward to use the best-fit Gaussian parameters to calculate the equivalent width, redshift, and column density of H I. To illustrate that we have extracted a reasonable distribution of lines, we plot the number of lines in our sample as a function of column density in Figure 1. The median redshift of the lines in our sample is $z = 2.35$. We have placed all of the lines between $10^{14.2}$ and $10^{16.2}$ cm^{-2} into a single bin since the column densities of these strongly saturated lines are poorly determined. In principle, we could use higher-order Lyman lines to measure the column density. Unfortunately, for most of the Lyα features in our sample, the corresponding Lyβ feature is either in the low wavelength portion of the Keck data, where the S/N is low, or at wavelengths in between the Keck and FOS spectral coverage where we have no data.

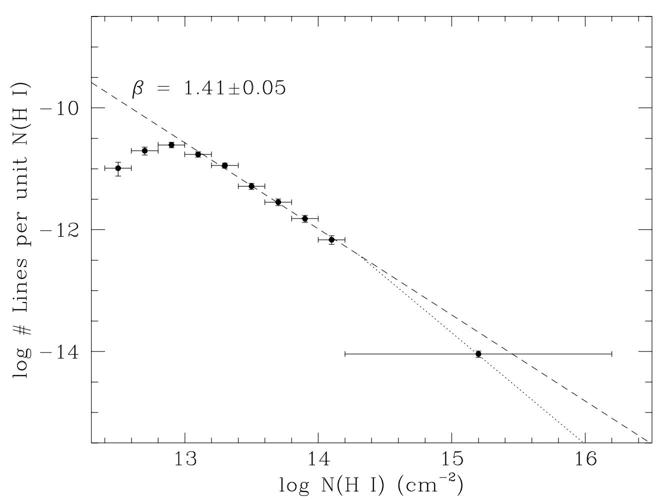

FIG. 1.— Distribution of the number of lines in our sample with column density. The dashed line is our best fit to the distribution between 10^{13} and $10^{14.2}$ cm^{-2} with $\beta = 1.41 \pm 0.05$. The dotted line represents $\beta = 1.83$ connecting to our best fit at $10^{14.3}$ cm^{-2}.

The ordinate in Figure 1 is proportional to the column density distribution function, often called $f(N)$ in the literature. As is standard practice, we fit the distribution between $10^{13.0}$ and $10^{14.2}$ cm^{-2} with a power law, $f(N) \propto N^{-\beta}$. Our best-fit power-law index is $\beta = 1.41 \pm 0.05$, plotted as the dotted line in Figure 1, in agreement with Kim et al. (1997) for this range of column densities at $z \approx 2.3$. The fit appears to be good down to 10^{13} cm^{-2}, which argues that we are essentially complete to this column density. The column density distribution function is known to steepen above $10^{14.3}$ cm^{-2} (Kim et al. 1997). We adopt $\beta = 1.83$ as found by Petitjean et al. (1993) to be a good fit between $\sim 10^{14}$ and 10^{16} cm^{-2}. We connect this distribution to our best fit at $10^{14.3}$ cm^{-2} and plot it as the dotted line in Figure 1. Clearly this agrees well with our high-column-density point. When considering the distribution of column densities for $N(\mathrm{H\ I}) > 10^{14.3}$ cm^{-2} which is important for our data simulations in §5.3, we therefore adopt $\beta = 1.83$ as representative of our data.

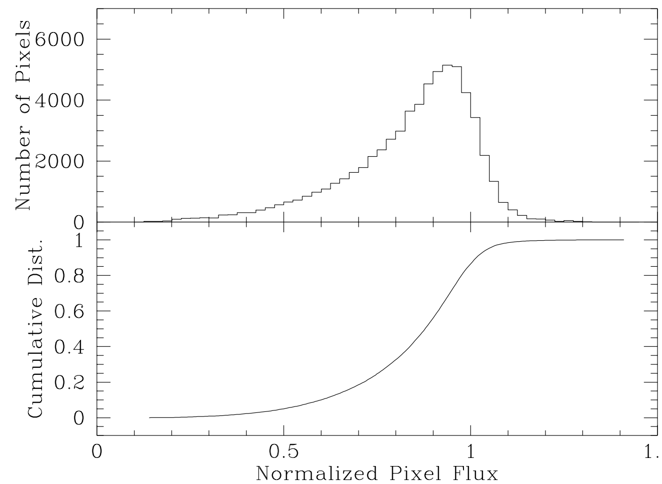

FIG. 2.— *Top*: Distribution of individual pixel fluxes in the FOS data of the four QSOs, after the spectra have been normalized and resampled into 0.1 Å bins. *Bottom*: The same distribution displayed as a cumulative distribution.

3.2. *Combination Technique*

The process of creating composite absorption spectra is conceptually straightforward. First we combine the G190H and G270H spectra into a single spectrum so that the wavelengths in the overlap region do not receive double weighting. To facilitate this, we resample the individual spectra into 0.1 Å bins in the observer frame – a factor of several smaller than the original pixels so as not to alter the character of the data. Then we normalize the FOS spectra to the continuum using a cubic spline in the same way as we did for the optical data. Instrumental artifacts and a damped Lyα absorption feature in one object are masked out. We also remove the noisy portion at the short wavelength end of the G190H data, below ~ 1650 Å, where the sensitivity of the red Digicon detector becomes low and the S/N drops per original FOS pixel drops below 5.

For each Lyα forest feature in the particular sample, the combined FOS spectrum of that object is shifted into the rest frame of the absorber by dividing the wavelength scale by $1 + z_{\mathrm{abs}}$. These shifted spectra are then rebinned into a common wavelength scale in the absorber frame for coadding. For convenience we choose a bin size of 0.1 Å, which corresponds to 48 km s^{-1} in the region of O V λ630, slightly smaller than the typical pixels in the original data.

For each pixel in the proposed composite spectrum, we then have a distribution of pixel fluxes from the individual shifted spectra. A crucial question remains – what statistic of this distribution do we use as the composite flux in order to optimize the sensitivity of our measurements? The answer depends strongly on the character of the noise, which in our study is due largely to random absorption features. If we were dealing with high S/N data and the continuum in the spectral region of interest were not polluted by random absorption lines, as is typical in searches for weak C IV absorption, then the noise would be Gaussian distributed and a mean or median combination method would do nicely to minimize the noise in the result. However, when the features of interest are strongly blended into the Lyα forest the noise is distinctly non-Gaussian.

On the top of Figure 2 we plot as a solid line the histogram of the pixel fluxes of the FOS spectra of our four QSOs, after the G190H and G270H data have been binned to 0.1 Å and combined. Clearly the pixels have a very asymmetric distribution in flux with a long tail to low flux due to the many absorption lines. We expect that at any random wavelength, where there is no feature, the contribution to the composite from the individual shifted spectra will consist of a random sampling from this distribution. We would like to maximize the S/N in these random samplings, which for our composite spectra corresponds to the S/N in the continuum. We can take any general percentile of the data by linearly interpolating the cumulative distribution, where the lowest flux at a given pixel is defined as the zeroth percentile and the highest flux as the 100th. The simplest and most common example is the median or 50th percentile, but we will show that we can increase the S/N significantly by making a different choice.

The optimal percentile should be near the peak of the distribution, which one can see from the cumulative distribution in Figure 2 is around the 80th percentile. We perform Monte Carlo simulations to show explicitly that this is the case. We take 100000 random samplings of 100 points from the flux distribution, each time calculating the nth percentile of the sample. Figure 3 shows the result of the simulations as a function of percentile, where the S/N is defined as the average value of the nth percentile of the sample divided by the rms deviation. Indeed, we see that the S/N peaks where the flux distribution peaks, with the optimal choice being the 79th percentile. An earlier version of these simulations led us to conclude that the 78th percentile was optimal which was used in the subsequent analysis. Since Figure 3 shows that the difference is negligible (a 0.3% difference in S/N), we use 78th percentile spectra for this work. The 78th percentile yields a S/N nearly 40% greater than the median in these simulations. The mean yields a S/N of 49.1, similar to the median. The optimal percentile is not a general result, but rather is peculiar to the S/N and absorption line density of our data. This discussion gives our method a solid statistical basis and points out clearly the importance of carefully considering the noise distribution of a particular dataset in order to maximize the resulting S/N in the composite. In §4 we will demonstrate empirically that taking the 78th percentile of the distribution is indeed essentially optimal for our data.

Since we have selected our QSO sample to search for O V λ630, we have FOS data at this wavelength for virtually all of the Lyα absorbers on our sample, the only exceptions being those few for which the wavelength of the O V absorption happens to lie in a masked region. Overall, we have FOS data for over 90% of the absorbers for rest-frame wavelengths between 560 and 890 Å. At wavelengths longer that $\sim$ 900 Å, the S/N in the composites becomes very low due to the high density of Lyman lines. As a result, we cannot place any interesting constraints on metal lines at these wavelengths. There are some interesting lines shortward of 560 Å, including O IV $\lambda\lambda$553, 554 and Ne VI λ559. Although we could use this O IV doublet to constrain the amount of O IV, we concentrate on O IV λ788 because it provides comparable sensitivity and we have data for more of the absorbers. For all other ions that we consider there is a single obvious choice for which line to use.

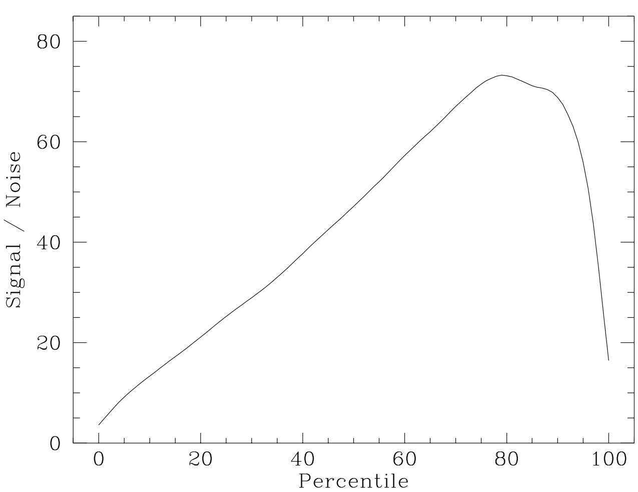

FIG. 3.— Average S/N of 100000 random samplings of 100 points from the distribution of all the pixel fluxes from the FOS spectra shown in Figure 2, as a function of the percentile taken for each sample.

3.3. *Wavelength Calibration*

There is a well-documented problem with the absolute wavelength scale of the FOS (Rosa et al. 1998). A solution to this problem has been found for data from the blue detector, which has a systematic shift over time, but a fix for the red detector data has not yet been established. We determine this empirically for our data. First, we find the relative shift between the G190H and G270H data for each QSO. Using data in the region of wavelength overlap from around 2220–2310 Å, we calculate, to the nearest 0.01 Å, the wavelength shift which minimizes the rms deviation of the pixels. We then shift the G190H data by the required amount and combine the two into a single spectrum. This method works well and gives shifts consistent with what we estimate by measuring individual features in the overlap region.

The overall shift of the combined G190H / G270H data on an absolute scale is more difficult to determine. Given the S/N of the data, Galactic absorption lines are not readily identifiable for HE 1122–1649 and HE 2347–4342, and only a few for HS 1103+6416 and HS 1700+6416, so in general using the Galactic lines is not a reliable way to set the wavelength scale. To estimate the overall shift, we create composite absorption spectra of the individual objects using only Lyα forest lines with Lyα equivalent widths > 0.5 Å. The lower limit was chosen so that a well-defined O V line could be seen for each object. In each case, a strong absorption feature occurs near the expected position of O V λ630, but slightly shifted by up to $\sim$ 100 km s^{-1}. We shift the FOS spectra by the amounts listed in Table 1 to center the O V feature as near as possible to 629.73 Å. The shifts listed for the G190H data include both the overall shift and that necessary for agreement with the G270H data. The required shifts are modest and well within the errors of the FOS red detector. We use these shifted spectra for all of our final results. To check the accuracy of the applied shifts, we generate a composite using absorbers with Lyα equivalent widths > 0.6 Å for each object. The larger lower limit makes some lower-ionization lines more visible, as discussed in §4.3. For each object, we have measured the positions of other lines for which we have data and that are strong enough to make an accurate determination of the wavelength centroids. For this purpose we use lines from the following list: Lyβ, Lyγ, Lyδ, He I λ584, O IV λ554, and O IV λ788. We find that the average shift of the lines for each object is < 40 km s^{-1}. Thus, the residual uncertainty in the wavelength scale is significantly less than the instrumental resolution and should have little effect on our results.

One may argue that by applying these shifts we could be artificially enhancing the O V feature, since we have used O V to set the wavelength scale. This may be so, but we point out that such an argument would apply only to O V and only for absorbers with a Lyα equivalent width > 0.5 Å. Our important results are derived almost entirely from weaker lines, and there is very little overlap between the relatively weak absorbers we analyze in detail and the strong systems we use to set the wavelength scale.

3.4. *Measuring the Equivalent Width*

To measure the equivalent widths of the composite absorption features we use the profile weighting method as described by Lu (1991). Since this is a crucial part of our analysis we describe it briefly here. For an unresolved absorption feature, if we know the instrumental line profile and the central wavelength of the feature, then in principle every pixel gives an estimate of the absorption equivalent width. To get an accurate measurement of the equivalent width, we should take a weighted mean of the individual pixel estimates of the equivalent width. If the error is constant as a function of wavelength, which is roughly true for our data, the optimal weighting is the square of the instrumental profile. The equivalent width is then calculated as

$$\mathrm{EW} = \frac{\sum(1 - f_i/c_i)p_i}{\sum p_i^2}, \tag{2}$$

where f_i is the flux, c_i is the continuum level, and p_i is the normalized instrumental profile. For the instrumental profile we use a Gaussian with a full-width at half maximum derived from the composite Lyβ features, which we find to be typically around 290 km s^{-1}. For the continuum determination we use a simple linear regression fit to the flux between $\pm$2500 km s^{-1}, eliminating the region between $\pm$500 km s^{-1} where the feature lies.

This weighting technique yields accurate results by relying on the fact that every individual metal feature associated with the sample has not only the same observed profile shape, but also, for any given ion, the same wavelength centroid in the reference frame of the absorber. For our sample, we determine the redshift of the absorption systems from the Lyα absorption lines. As discussed in §3.3, the mean shift of absorption lines with respect to this reference frame due to uncertainties in the FOS wavelength scale is < 40 km s^{-1} for all four lines of sight. However, what are the uncertainties for individual absorbers? Ellison et al. (1999) find an rms dispersion in the velocity offset between C IV and H I absorption of 27 km s^{-1}, while Ellison et al. (2000) find a dispersion of 17 km s^{-1}. The authors point out that these offsets can have a dramatic effect on the results of the stacking technique when applied to high-resolution data, such as that from the Keck HIRES. However, at the FOS resolution, typical offsets of 17–27 km s^{-1} should have little effect on the composites.

4. RESULTS

We divide our analysis into three groups based on the Lyα feature strength. One group consists of the Lyα lines with N(H I)$< 10^{14.2}$ cm^{-2}. These lines are unsaturated and therefore we have accurately measured column densities, so the analysis requires fewer assumptions than for saturated lines. This is the most important group because it samples absorbers for which little information is available about metal content. For stronger lines, we cannot reliably measure the column density of H I, so we must instead discriminate absorbers by Lyα equivalent width. We divide the stronger lines into two groups – an intermediate sample with Lyα equivalent widths $\lesssim 0.6$ Å, and a sample with Lyα equivalent widths $\gtrsim 0.6$ Å. Although the exact division is somewhat arbitrary, this strongest group consists of lines with H I column densities $\gtrsim 10^{15}$ cm^{-2}, which are generally associated with metal-line systems. Each group thus spans roughly an order of magnitude in column density. We will discuss the low-column-density sample first, since these weak lines are useful for assessing the success of our composite technique.

4.1. *Low Column Densities: N(H I)$< 10^{14.2}$ cm^{-2}*

It is not obvious a priori at what H I column density we should place the lower limit of our sample to achieve the most secure detection, and in fact this depends on the unknown strength of the feature. One would like to include many lines to increase the S/N, but this involves adding in lines of lower and lower column density. At some point, the feature will become so weak that including more lines essentially adds only noise, thereby reducing the significance of any detection. As pointed out by Lu (1991), there should therefore be some optimal lower limit which maximizes the S/N of the result. To find the optimal detection, we let the lower limit range from $10^{13.0}$ to $10^{13.9}$ cm^{-2}. The resulting 78th percentile spectra are shown in Figure 4 in the velocity space of the O V λ630 feature. The number of lines and the O V equivalent width for each sample, measured as described in §3.4, are listed in Table 2. One can clearly see how the noise is reduced by including more lines, and the O V feature becomes well-defined. In none of the samples do we find any evidence for O IV λ788.

In order to assess the errors on these results and their significance, we perform Monte Carlo simulations in which we randomize the redshifts of the Lyα features so that they can take on any value in the allowable range, i.e., between Lyβ and 5000 km s^{-1} blueward of Lyα for the particular object, as defined previously. The resulting composites should thus consist of random noise, and by measuring the equivalent widths in the simulated spectra in the same way as for the real data, we can evaluate the errors on our equivalent width measurements. We have performed 1000 simulations for each sample, and the rms deviations of the equivalent width in these Monte Carlo spectra are shown as the errors on the O V equivalent width in Table 2. The mean equivalent width in these simulations is slightly less than zero, typically by -0.5 mÅ, indicating that there is a slight zero-point offset associated with our measurement technique that is likely due to the continuum placement. Because for our analysis we compare our results to simulated data, which also include this effect, we do not add it into our measurement of the line equivalent width.

Table 2
O V EWs for Weak Lyα absorbers: N(H I)$< 10^{14.2}$ cm^{-2}

$\log N_{\rm min}$ (H I)	n	O V EW (mÅ)	$P_{\rm real}$
13.9	69	19.0 ± 8.9	0.976
13.8	96	15.7 ± 7.4	0.987
13.7	136	17.3 ± 6.2	0.995
13.6	163	14.2 ± 5.5	0.996
13.5	203	14.9 ± 5.0	>0.999
13.4	243	10.8 ± 4.8	0.987
13.3	298	12.5 ± 4.1	0.998
13.2	347	10.9 ± 3.7	0.999
13.1	394	8.5 ± 3.7	0.987
13.0	444	7.3 ± 3.3	0.956

Table 3
Effect of Percentile on O V Feature Significance

Percentile	O V EW (mÅ)	$P_{\rm real}$
0	132.4 ± 148.9	0.778
10	-0.4 ± 24.7	0.568
20	7.0 ± 13.3	0.820
30	12.5 ± 11.3	0.904
40	13.0 ± 8.7	0.950
50	11.1 ± 7.2	0.957
60	10.6 ± 5.9	0.970
70	11.7 ± 5.0	0.995
80	9.7 ± 3.6	0.997
90	7.9 ± 3.8	0.986
100	14.6 ± 16.5	0.813

These simulations can also be used to answer the question of how likely it is that the feature is due to random chance. In column 4 of Table 2, we list the fraction of simulated equivalent widths that were less than that measured

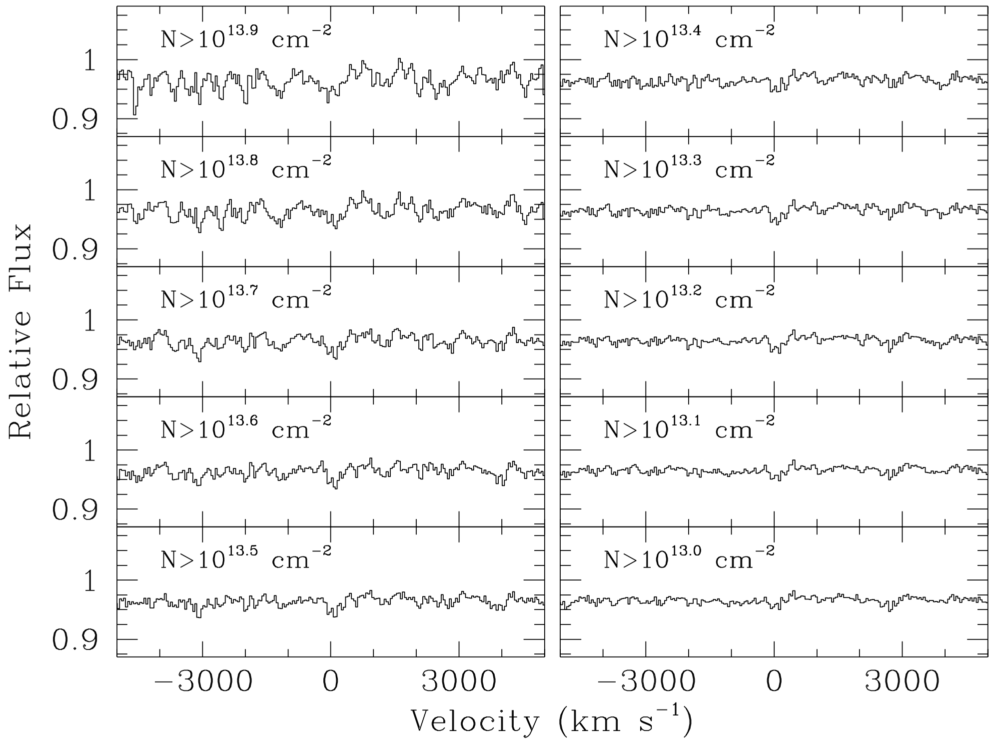

FIG. 4.— Composite spectra of Lyα forest features with N(H I)$< 10^{14.2}$ cm^{-2} for various minimum H I column densities, plotted in the velocity space of O V λ630.

in the real data, which can be interpreted as the probability that the result is not due to chance. For a lower limit of $10^{13.5}$ cm^{-2}, none of the simulations exceeded the measured value, so we list the probability as > 0.999. The significance maximizes with a lower limit around $10^{13.2}$ to $10^{13.7}$ cm^{-2}. Because so few (two or fewer) of the simulations exceed the real measurements for lower limits of $10^{13.2}$, $10^{13.3}$, and $10^{13.5}$ cm^{-2}, we cannot reliably distinguish which is of greater significance. However, we find that the distribution of equivalent widths in the simulations are well-described by a Gaussian, and therefore one can simply use Gaussian statistics to estimate the significance. The best detections correspond to approximately a 3σ fluctuation above the mean noise level and are significant at greater than a 99% confidence level.

Since the low-column-density samples contain many lines, we can use them to illustrate the validity of our choice of taking the 78th percentile in forming the composite spectrum. As our test case we use the N(H I)$> 10^{13.2}$ cm^{-2} sample. At the top of Figure 5, we show the 78th percentile spectrum with 347 lines in the sample. Below this, we show various other percentiles of the contributing spectra, from the 10th (lowest) to the 90th (highest), plotted at true scale. We can measure the equivalent width of the feature in each percentile and calculate the noise with Monte Carlo simulations as before. These results are shown in Table 3. As expected, although the equivalent width of the feature is roughly constant, the noise varies considerably. The gain in S/N by using the 78th percentile over, for example, the median is even greater than what would be expected based on our simulations in §3.2. This is probably because the noise is due mostly to

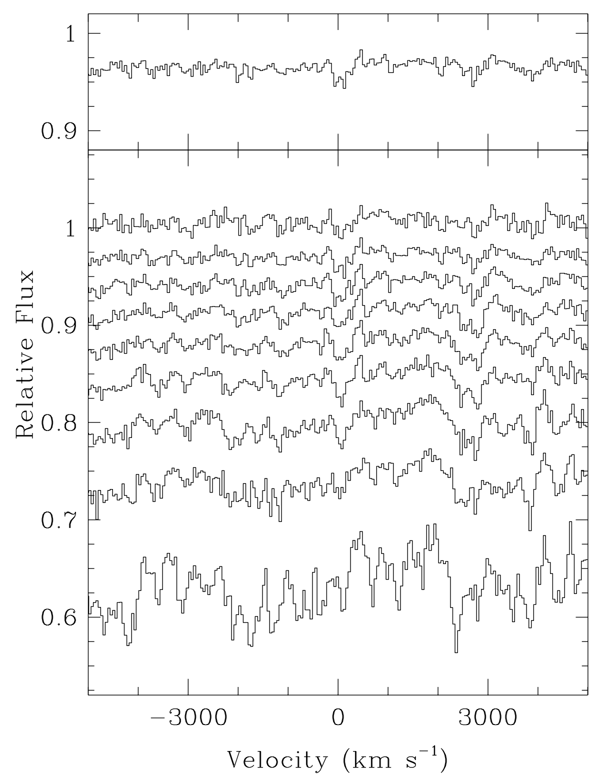

FIG. 5.— *Top*: Composite 78th percentile spectrum of all lines with $10^{13.2} < N$(H I)$< 10^{14.2}$ cm^{-2} plotted in the velocity space of O V λ630, as shown in Figure 4. *Bottom*: Various percentile spectra of the same data showing the effect of the percentile on the result. The spectra are in steps of 10 percent, ranging from the 10th percentile (bottom) to the 90th percentile (top).

random absorption features which span several pixels and thus cause correlated errors in the continuum. We list the significance of the detection in each percentile in Table 3, and none of these exceed the significance achieved with the 78th percentile, although the results are similar for the 80th percentile. Based on the simulations in §3.2 and the success of the 78th percentile when applied to the real data, we feel justified in using this technique.

4.2. *Intermediate Column Densities:* $10^{14.2} < N(H\,I) \lesssim 10^{15}$ cm^{-2}

The division between the Lyα forest and metal-line systems is not a precise concept. In examining the intermediate-column-density lines we therefore try a range of upper limits on the Lyα equivalent widths. The measured equivalent widths of O V are listed in Table 4. The spectra are shown in Fig 6, where we display not only O V but also O IV λ788 to illustrate that there is no evidence for a detection, which we quantify in §4.4. As opposed to the way we analyzed the low-column-density lines, here as we include more lines we are including lines of increasing strength and thus we definitely expect the significance of the detection to increase. This is clearly the case, and with a Lyα EW upper limit of 0.6 Å we can detect O V with $> 4\sigma$ confidence.

4.3. *High Column Densities:* $N(H\,I) \gtrsim 10^{15}$ cm^{-2}

For a b-parameter of 30 km s^{-1}, a Lyα EW of 0.6 Å corresponds to an H I column density of $10^{16.0}$ cm^{-2}. Since we excluded systems with column densities $\gtrsim 10^{16.2}$ cm^{-2} based on Lyman-limit detections, lines with a Lyα EW $\gtrsim 0.6$ Å must be high-column-density systems with large b-parameters, and we expect them to be associated with traditional "metal-line systems". Although these strong systems are scarce and not the primary interest of this work, we can detect many absorption lines at such large column densities which further illustrates the success of our technique.

Table 4

O V EWs for Intermediate Lyα Absorbers: $10^{14.2} < N(\mathrm{H\,I}) \lesssim 10^{15}$ cm^{-2}

Max Lyα EW (Å)	n	O V EW (mÅ)	$P_{\rm real}$
0.4	20	37.8 ± 19.1	0.962
0.5	36	48.3 ± 13.9	0.998
0.6	49	45.3 ± 11.4	>0.999
0.7	55	48.2 ± 10.5	>0.999

In Figures 7–9 we show plots for O V λ630, O IV λ788, O IV λ554, O IV λ608, O III λ833, and He I λ584. These lines have all been observed on an individual basis in Lyman-limit systems (Reimers & Vogel 1993; Vogel & Reimers 1993) and metal-line systems (Vogel & Reimers 1995). The measured equivalent widths with errors from Monte Carlo simulations are listed in Table 5. The O IV line at 554.07 Å has a weaker doublet companion at 553.33 Å which is visible in Figure 8. We measure only the equivalent width of the λ554 line, although the presence of the λ553 line probably affects this measurement slightly. All of the lines are detected with fairly high significance (> 0.98) in the EW> 0.6–0.8 Å samples, with the exception of O IV λ608. By itself the presence of this line would be tenuous at best, but given the strength of the other O IV lines it is present at about the expected level.

4.4. *Limits on Other Ions*

Using the same Monte Carlo simulations that we used to determine error bars on the observed features, we can define 90% confidence limits on the equivalent widths of absorption for unobserved ions. We do this not only for O IV λ788 absorption but also for several other ions which have transitions which one might expect to observe in the EUV. Specifically, we constrain He I λ584, O III λ833, N IV λ765, Ne V λ568, Ne VI λ559, Ne VIII λ770, and Mg X λ610. We concentrate on three specific samples: (1) the absorbers with $10^{13.2} < N(\mathrm{H\,I}) < 10^{14.2}$ cm^{-2}, which we refer to as sample L or the low-column-density sample, (2) the absorbers with $N(\mathrm{H\,I}) > 10^{14.2}$ cm^{-2} and Lyα equivalent widths < 0.6 Å, which we will to as sample I or the intermediate-column-density sample, and (3) the absorbers with Lyα equivalent widths > 0.6 Å, which we refer to as sample H or the high-column-density sample. The equivalent width limits for various unobserved ions are listed in Table 6 for all three samples. For completeness we include the measured equivalent width for detected ions. The ratios of the these ions to H I are discussed in §5.

5. DISCUSSION

5.1. *The O V / H I Ratio*

The interpretation of composite spectra is not straightforward. In order to reliably interpret the measured equivalent widths, it is necessary to generate simulated data to compare to the results. As a simplification, we first will assume that the mean ratio $\langle \mathrm{O\,V/H\,I} \rangle$ is constant within each of our subsamples. This may or may not be a good assumption, depending on the ionization model, although our subsamples span a small enough range of $N(\mathrm{H\,I})$ that we do not expect $\langle \mathrm{O\,V/H\,I} \rangle$ to vary by more that a factor of ~ 2. Making this assumption allows us to derive results that are, as much as possible, model independent. Later in this section we will drop this restriction and simulate data using particular ionization models. Our Monte Carlo simulations proceed as follows:

1. We randomize the redshift of each line to take on any value in the allowable range, as we did for our noise simulations in §4.

2. We calculate the O V column density for each absorber from the H I column density and the given relative abundance $\langle \mathrm{O\,V/H\,I} \rangle$.

3. The equivalent width of O V λ630 is calculated from the O V column density assuming a particular b-parameter.

4. For the particular (randomized) redshift of each absorber, we insert a Gaussian absorption feature with a FWHM of 290 km s^{-1} and the appropriate equivalent width at the position of the O V λ630 absorption.

5. The absorbers are combined into a composite and the equivalent width of O V λ630 is measured as we have done for the real data.

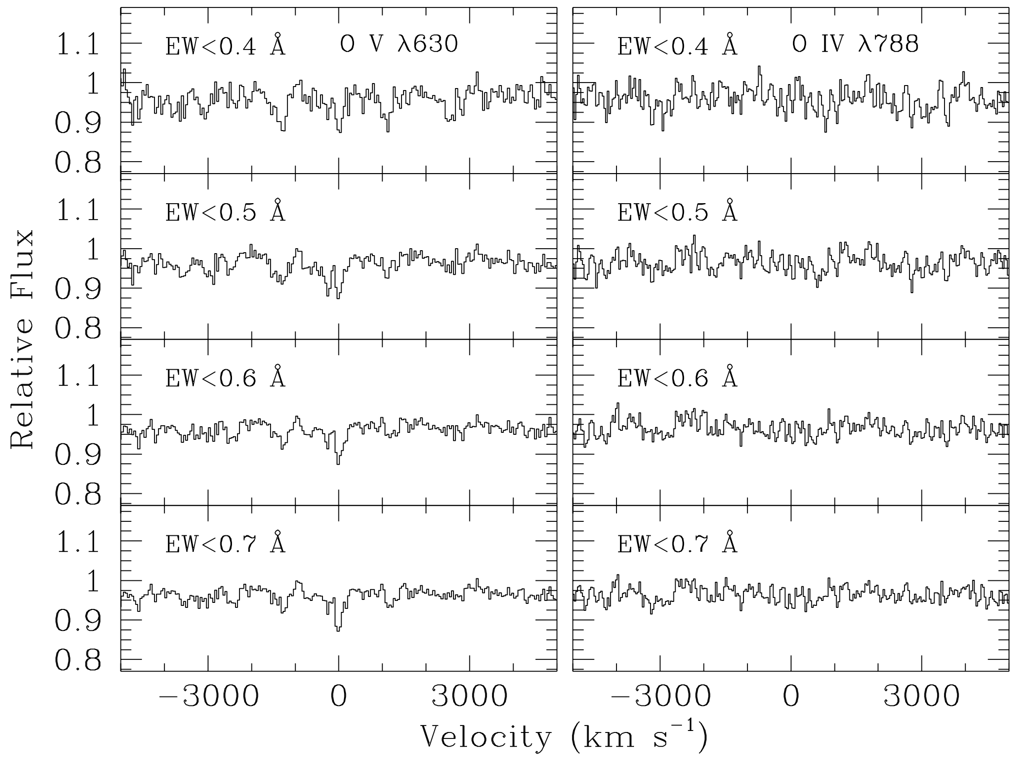

FIG. 6.— Composite spectra of Lyα forest features with N(H I)$> 10^{14.2}$ cm^{-2} for several maximum Lyα equivalent widths. The region for O V λ630 is plotted on the left, while the corresponding O IV λ788 region is shown on the right. The O IV λ788 feature is not detected in any of these spectra.

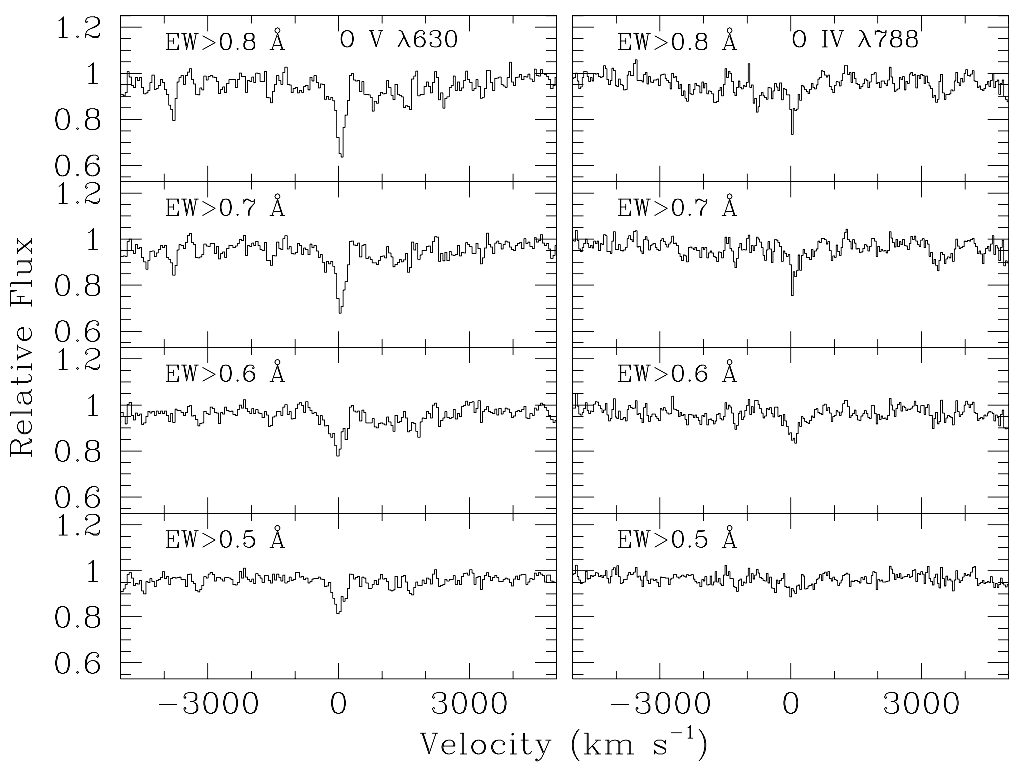

FIG. 7.— Composite spectra of the strongest Lyα forest features in our sample for several minimum Lyα equivalent widths. O V λ630 is shown on the left, O IV λ788 on the right.

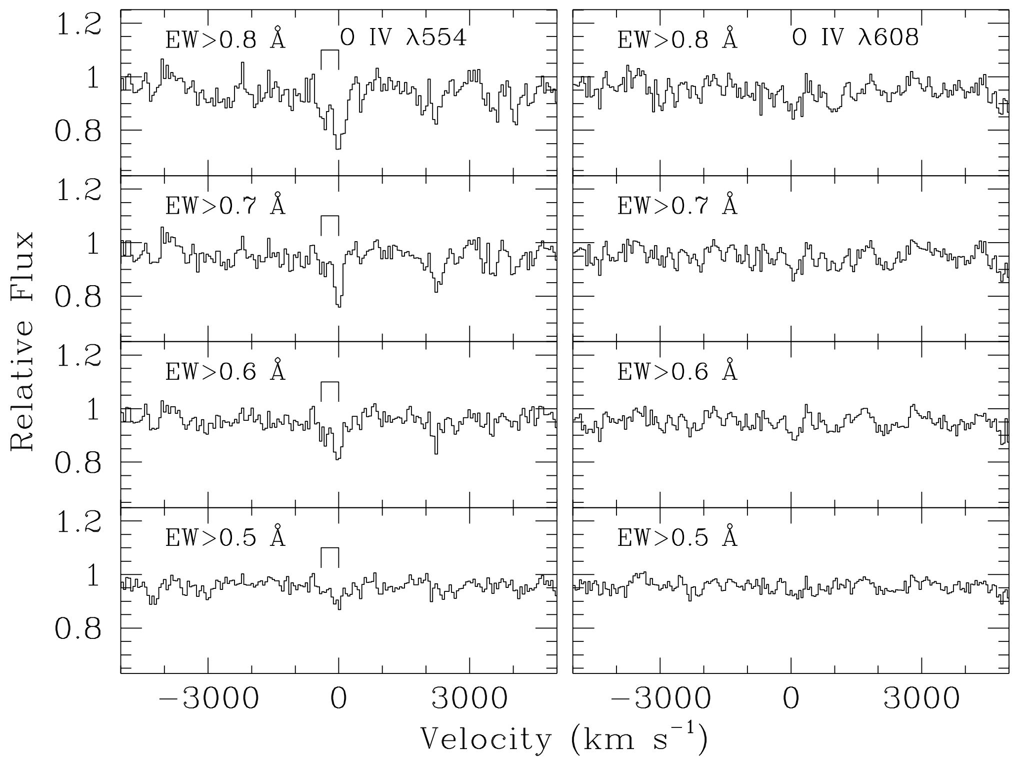

Fig. 8.— Same composites as Figure 7, except O IV λ554 is shown on the left and O IV λ608 on the right. The O IV spectra are plotted in the velocity space of the 554.07 Å line. Above the O IV spectra we indicate the positions of this line and the doublet companion at 553.33 Å.

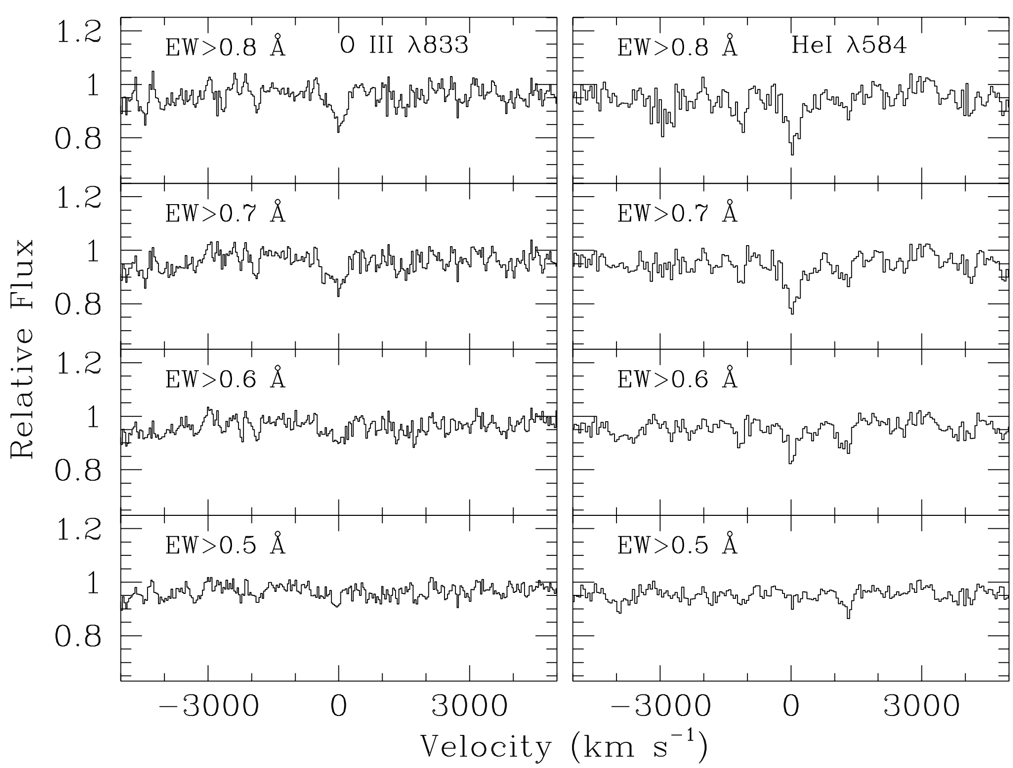

Fig. 9.— Same composites as Figures 7 and 8 with O III λ833 shown on the left and He I λ584 on the right.

Table 5
O V, O IV, O III, and He I EWs for Strong Lyα Absorbers: N(H I)$\gtrsim 10^{15}$ cm^{-2}

		Equivalent Width (mÅ)					
Min Lyα EW (Å)	n	O V λ630	O IV λ788	O IV λ554	O IV λ608	O III λ833	He I λ584
0.8	11	156.6 ± 25.6	97.3 ± 39.2	124.3 ± 34.6	52.3 ± 28.6	120.9 ± 45.2	110.3 ± 29.7
0.7	14	146.1 ± 21.7	91.2 ± 36.7	68.6 ± 28.7	30.4 ± 25.2	113.8 ± 40.4	111.0 ± 25.1
0.6	20	99.6 ± 18.4	92.2 ± 27.7	77.3 ± 22.7	32.9 ± 21.3	62.7 ± 30.5	64.0 ± 20.5
0.5	33	85.7 ± 13.7	44.8 ± 21.5	49.2 ± 17.2	19.0 ± 15.6	29.6 ± 22.9	4.7 ± 15.4

Table 6
Equivalent Widths and Column Density Ratios to H I

		Sample L		Sample I		Sample H
Ion	λ (Å)	EW(mÅ)	$\langle X_i/\mathrm{H\ I}\rangle$	EW(mÅ)	$\langle X_i/\mathrm{H\ I}\rangle$	EW(mÅ)
He I	584.33	< 6.0	< -1.0	< 16.4	< -1.5	64.0 ± 20.5
N IV	765.14	< 6.2	< -1.5	< 23.3	< -1.9	< 37.0
O III	832.93	< 8.1	< -1.0	< 23.7	< -1.4	62.7 ± 30.5
O IV	787.71	< 7.0	< -1.0	< 18.8	< -1.5	92.2 ± 27.7
O V	629.73	10.9 ± 3.7	-1.6 to -0.6	45.3 ± 11.4	-1.7 to -0.8	99.6 ± 18.4
Ne V	568.42	< 5.1	< -0.7	< 16.6	< -1.0	< 26.3
Ne VI	558.59	< 7.9	< -0.7	< 20.1	< -1.1	< 31.2
Ne VIII	770.40	< 8.2	< -0.8	< 25.3	< -1.1	< 38.9
Mg X	609.79	< 4.8	< -0.6	< 17.2	< -1.0	< 28.4

An important assumption in this process is the b-parameter used to calculate the equivalent width. For the weak lines in the low-column-density sample, this is fairly unimportant, since most of the lines will be reasonably near the linear portion of the curve of growth. It will have some effect, though, and it is worth considering since this will have a more pronounced effect when we model lines at higher column densities. Individual metal lines as observed in C IV absorption typically have quite small b-parameters. As examples, Cowie et al. (1995) find a median b for C IV lines of 10 km s^{-1}, while Ellison et al. (2000) find a median b of 13 km s^{-1}. However, when the C IV absorption is strong, the absorption corresponding to particular Lyα features often consists not of a single line but several such narrow absorption features. The effective b-parameter for such metal-line clusters, when viewed as a single absorption feature, is significantly larger than 10 km s^{-1}. Because individual metal lines are not generally detected at the small H I column densities that we probe, we do not know the typical structure of the metal-line absorption. Strong C IV absorbers often contain perhaps 3–5 components (see, for example, the C IV profiles in Ellison et al. (1999)). An effective b-parameter of 50 km s^{-1} should therefore provide a reasonable extreme value for the typical b-parameter of the metal absorption associated with a sample of H I lines. To illustrate the effect of b on our results, we create simulated data for b-parameters of 10 and 50 km s^{-1}. A physically realistic picture is probably somewhere in between, since it seems likely that some absorbers will consist of several components whereas others may be dominated by a single strong component.

The simulations also depend on the scatter in $\langle$O V/H I$\rangle$ at fixed N(H I), which depends on the scatter in both the metal abundances and physical conditions of the absorbers. Using C IV absorption, Rauch et al. (1997) and Hellsten et al. (1997) find a scatter of around an order of magnitude, while the analysis of Davé et al. (1998) suggests that the true scatter may be smaller as some of the observed scatter could be attributable to fitting uncertainties. The individual systems measured by Ellison et al. (2000) indicate an rms scatter of around 0.5 dex. We generate simulated data with a Gaussian distribution in $\langle$O V/H I$\rangle$ with an rms scatter, which we denote as σ_{O}, of 0.0, 0.5, and 1.0 dex. The results of our simulations of sample L for different values of b and σ_{O} are plotted in Figure 10, compared with our observed value. For each line in Figure 10 we have computed 100 simulated data sets for each point in steps of 0.1 in $\langle$O V/H I$\rangle$, and the plotted value represents of the mean of these simulations. The b-parameter makes a small difference, but σ_{O} has a larger effect. If we assume that σ_{O} is likely in the range 0.5–1.0 and allowing for the uncertainty in b, we get agreement with our observations for $\langle$O V/H I$\rangle \approx -1.7$ to -0.8.

Generating simulated datasets for sample I is not as simple. Because we do not have accurately measured column densities for these lines, we cannot simply calculate the O V column densities from the H I column densities of the lines in our sample. Instead, we use simulated lists of random lines drawn from a column density distribution with $\beta = -1.41$ for N(H I)$< 10^{14.3}$ cm^{-2} and $\beta = -1.83$ for $10^{14.3} < N$(H I)$< 10^{16.2}$ cm^{-2}, as shown in Figure 1. We assume a b-parameter distribution as derived by Kirkman & Tytler (1997): a Gaussian distribution in b with $\bar{b} = 23$ km s^{-1} and $\sigma_b = 14$ km s^{-1}, and a minimum b given by $b_{\min} = 14 + 4 \times \log[N(\mathrm{H\ I})/12.5]$ km s^{-1}. The distribution of b is important because we have used a cut in equivalent width to define our sample, so we must know the equivalent width of the lines in the simulated data. In our full sample, we have 69 Lyα lines with $10^{14.2} < N$(H I)$< 10^{16.2}$ cm^{-2}. In Figure 11 we plot a histogram of the equivalent width distribution of these lines, as well as the average of 1000 simulated lists of Lyα lines in this column density range. The notable difference between the two is the excess of large equivalent width lines, EW $\gtrsim 0.8$ Å, in the real data. These are likely metal-line systems, as discussed earlier, though they could also be blended lines. The upper-limit in Lyα equivalent width of 0.6 Å for sample I is thus chosen to help assure that this sample is relatively free of metal-line systems. At lower equivalent widths, it seems that the simulated data are a good approximation of the real data.

In generating our simulated O V data for sample I, we replace our sample absorbers with randomly generated line lists. Given that we now have lines with a realistic distribution of H I column densities, we can calculate the O V column densities and generate simulated data as we did for the lower column densities. Figure 12 shows the results of the simulations. At these larger O V equivalent widths, σ_O makes less of a difference, but the results are quite sensitive to the assumed b-parameter, since for a small b-parameter the stronger lines will begin to saturate. An effective b-parameter of 10 km s^{-1} is almost certainly unrealistically low for this sample, since C IV absorption in this regime often shows structure, but it is useful to consider as an extreme case. Depending on the b-parameter, we find $\langle$O V/H I$\rangle$ should be in the range -1.6 to -0.6 for sample I. This agrees with what we derived for sample L, giving us confidence in our analysis and suggesting that $\langle$O V/H I$\rangle$ does not vary more than an order of magnitude over the range of H I column densities that we have considered, from $10^{13.2}$ to $\sim 10^{15}$ cm^{-2}.

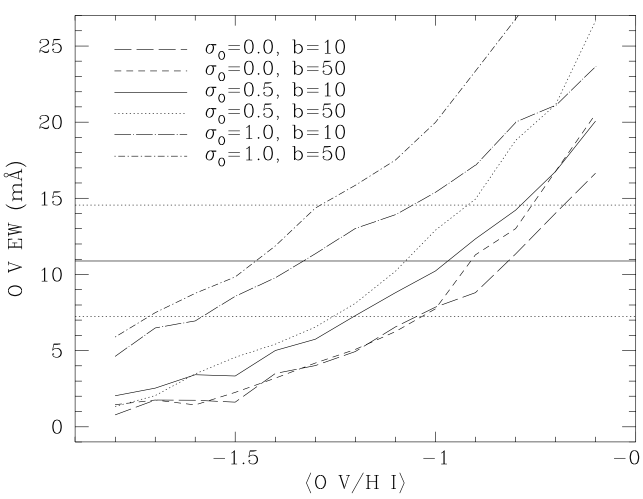

FIG. 10.— Expected O V equivalent widths from simulated data for Lyα absorbers with $10^{13.2} < N(\mathrm{H\,I}) < 10^{14.2}$ cm^{-2}, as a function of the mean ratio $\langle$O V/H I$\rangle$. The different curves correspond to different assumptions for the b-parameter for O V and the rms scatter in $\langle$O V/H I$\rangle$, denoted as σ_O. Our measured value is shown as the horizontal solid line, and the 1σ limits on the measured value are shown as the horizontal dotted lines.

5.2. *Other Ions*

To this point we have only analyzed O V since it is the only ion we detect in samples L and I. However, in §4.4 we placed 90% confidence limits on the equivalent widths of absorption from other ions. By creating model data as we have done for O V $\lambda630$, we can convert these 90% confidence upper limits on the equivalent widths of metal lines of other ions into constraints on the column density ratio of the corresponding ions to H I. For all of the ions we assume an rms scatter in $\langle$X$_i$/H I$\rangle$ of 0.5 dex for the simulated data. Table 6 lists our derived values and limits on $\langle$X$_i$/H I$\rangle$ for samples L and I. We do not calculate values for sample H because our lack of knowledge of the H I column densities makes the results very uncertain.

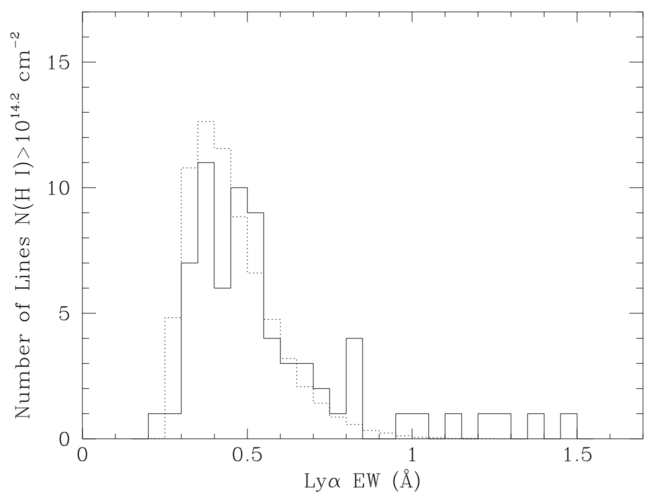

FIG. 11.— *Solid Line*: Distribution of rest-frame equivalent widths of the 69 Lyα absorption lines in our sample with H I column densities $> 10^{14.2}$ cm^{-2}. *Dotted Line*: Average distribution of rest-frame equivalent widths from 1000 randomly-generated lists of 69 Lyα lines with column densities $> 10^{14.2}$ cm^{-2}, assuming the column density distribution shown in Figure 1 and a b-parameter distribution as derived by Kirkman & Tytler (1997).

5.3. *The Oxygen Abundance*

Converting a value for the $\langle$O V/H I$\rangle$ into an oxygen abundance $\langle$O/H$\rangle$ requires knowledge of the relative ionization correction for the ions O V and H I. This is generally ascertained by means of photoionization models in which the IGM is illuminated by the processed radiation of QSOs and/or stars. We use the photoionization code CLOUDY (version 94.00; Ferland 1996). Because we have not resolved individual O V absorption components, in using these models to infer $\langle$O/H$\rangle$ we must necessarily assume that the absorbers are predominantly single-phase; i.e., the O V and H I absorption occurs in the same gas. The main inputs to the models are the density and temperature of the absorbers as a function of H I column density, and the shape and normalization of the ionizing continuum. For the physical conditions in the absorbers we use the results of Hellsten et al. (1998), which are based on hydrodynamical simulations as described by Katz, Weinberg, & Hernquist (1996). At $z = 3$, Hellsten et al. (1998) find that the typical density of the absorbers in their model are well-described by a simple analytic fit, $\log n_{\mathrm{H}} = -14.8 + 0.7 \log N(\mathrm{H\,I})$ assuming $\Omega_b h^2 = 0.0125$. The typical temperature of the absorbers is described by $\log T = 7.17 + 0.65 \log n_{\mathrm{H}}$ for $\log n_{\mathrm{H}} < -3.8$ and $\log T = 3.18 - 0.4 \log n_{\mathrm{H}}$ for $\log n_{\mathrm{H}} > -3.8$. The temperature relation is somewhat dependent on the ionization history of the universe (Hui & Gnedin 1997), particularly for underdense gas, but for the absorbers and redshifts we are studying this is a small effect and our results are fairly insensitive to the temperature.

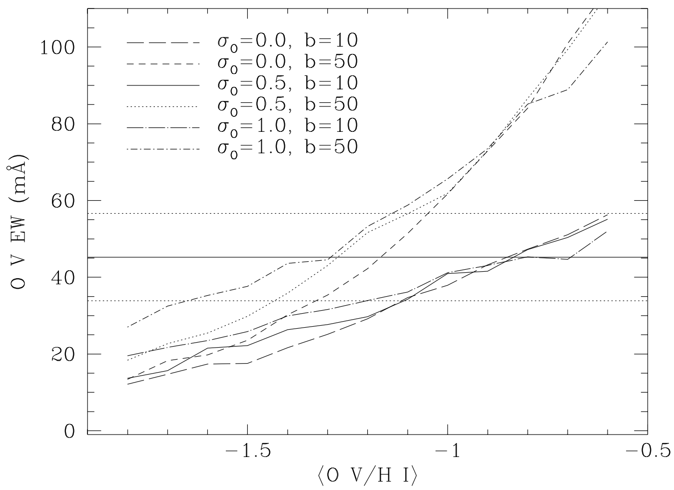

FIG. 12.— Same as Figure 10 but for absorbers with $N(\mathrm{H\,I}) > 10^{14.2}$ cm^{-2} and a Lyα equivalent width < 0.6 Å. In contrast to the weaker lines in Figure 10, the scatter σ_{O} makes only a small difference but the result is more sensitive to the assumed b-parameter, since many of the O V features would begin to saturate if b were small.

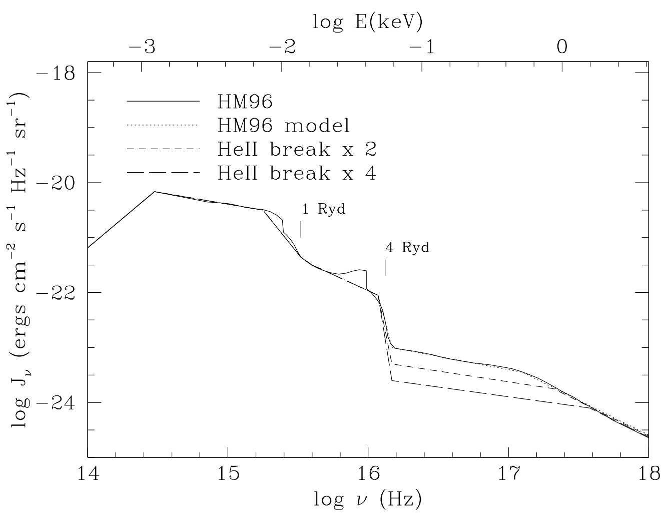

FIG. 13.— Various ionizing spectral shapes considered in this work. The solid line shows the spectrum of Haardt & Madau (1996) at $z = 2$. The dotted line shows an approximation to this spectrum using just a few points. These two spectra yield virtually indistinguishable results for the ions we consider. The dashed lines show the same model spectrum, except we have artificially increased the break at the He II ionization edge by factors of two and four.

For our nominal ionizing spectrum we use the standard Haardt & Madau (1996, hereafter HM96) spectrum. Specifically, we use their result for $z = 2$, although there is very little evolution in this spectrum between $z \sim 2$ and 3. HM96 assume that QSOs are the source of the ionizing radiation for the IGM. They assume a QSO spectral index of $\alpha_{\mathrm{EUV}} = -1.5$ ($f_\nu \propto \nu^\alpha$) for the continuum shortward of the Lyman limit, consistent with the $\alpha_{\mathrm{EUV}} = -1.57 \pm 0.17$ for radio-quiet QSOs derived by Telfer et al. (2002). Some recent hydrodynamical simulations of the IGM, however, suggest that a softer ionizing continuum than HM96 is necessary to explain the observed ratio of He II to H I in the IGM. Zhang et al. (1997) require less He II ionizing radiation by a factor of ~ 4, while Theuns et al. (1998) require a factor of ~ 2 less. Croft et al. (1997) resolve the discrepancy by increasing $\Omega_b h^2$ by an amount consistent with recent determinations of $\Omega_b h^2$ from D/H (O'Meara et al. 2001) and the cosmic microwave background (de Bernardis et al. 2002). Because the ions of interest to our discussion, in particular O V, are created by photons with wavelengths shortward of the He II break, our results are sensitive to differences in the He II photoionization rate. We create different ionizing spectra for our photoionization models by first creating a simple analytic fit to the HM96 spectrum, which we find produces indistinguishable results for the ions of interest. We then create softer spectra by simply increasing the strength of the break at the He II edge and then extending the softer spectrum to where it meets the HM96 spectrum in the X-ray regime. The original HM96 spectrum and our model spectra are shown in Figure 13. For all these models we adopt the normalization of the ionizing continuum of $J_\nu = 10^{-21.3}$ ergs cm^{-2} s^{-1} Hz^{-1} sr^{-1} at 1 Ryd as derived by HM96 and in good agreement with Giallongo et al. (1996).

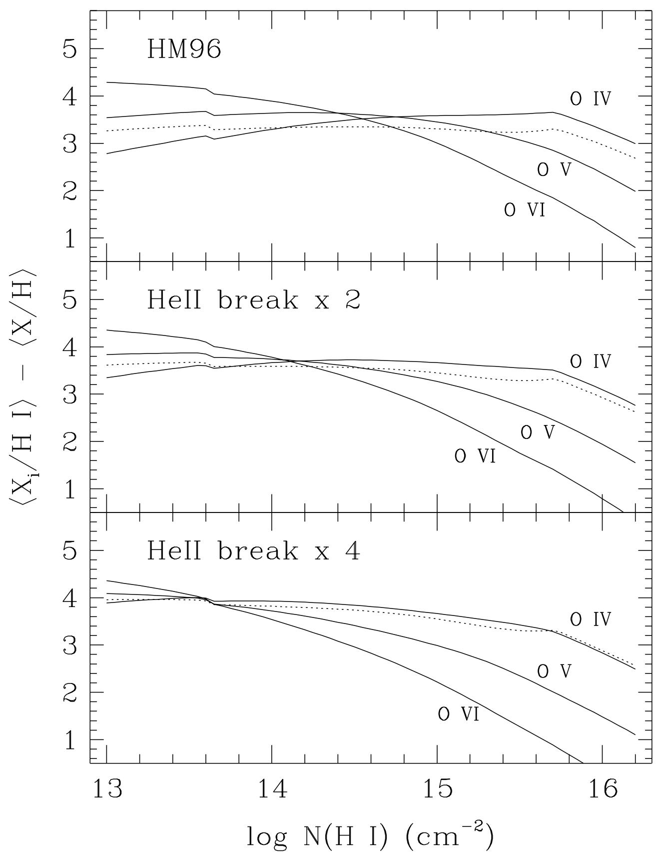

FIG. 14.— Ionized fractions of various ions relative to H I. The solid lines are for O IV–O VI and are labeled in the diagram. The dotted line is for C IV. The models correspond to the ionizing spectra shown in Figure 13. A normalization of $J_\nu = 10^{-21.3}$ ergs cm^{-2} s^{-1} Hz^{-1} sr^{-1} at 1 Ryd is used for all three models.

In Figure 14 we plot the ionized fractions of O IV, O V, O VI, and C IV relative to H I for our photoionization models. For the HM96 spectrum, ⟨O V/H I⟩−⟨O/H⟩ remains relatively constant for $10^{13} < N(\mathrm{H\,I}) < 10^{14.8}$ cm^{-2} at around 3.6. Given our values of ⟨O V/H I⟩ for sample L, this implies ⟨O/H⟩ around -5.3 to -4.4, or [O/H] around -2.2 to -1.3 with respect to the standard solar oxygen abundance. In the softer ionizing spectra models, slightly less oxygen is required to explain our measurement for sample L but slightly more oxygen for sample I. At larger H I column densities, $\langle$O V/H I$\rangle$ varies more dramatically with N(H I) and the interpretation of our measured value of $\langle$O V/H I$\rangle$ over a range of N(H I) is less obvious.

To include the effect of a changing ionization state with N(H I), we create simulations using these specific ionization models to determine N(O V) for the simulated absorption where the free parameter is now $\langle$O/H$\rangle$ rather than $\langle$O V/H I$\rangle$. We calculate model equivalent widths for O IV λ788 as well to compare with our limits since this can provide an interesting constraint on the ionization state. In Figure 15 we plot the equivalent widths of O V and O IV as a function of $\langle$O/H$\rangle$ for sample L, assuming $b = 50$ km s^{-1} and $\sigma_{\rm O} = 0.5$ dex. We do not plot the results for different values of the b-parameter and $\sigma_{\rm O}$, but the effects are very similar to those seen in Figure 10; i.e., the required $\langle$O V/H I$\rangle$ is more by around 0.1 for $b = 10$ km s^{-1}, and less by around 0.4 for $\sigma_{\rm O} = 1.0$ dex. As expected, the required $\langle$O/H$\rangle$ agrees with what we estimated above, with slightly less oxygen required for the softer spectra. For none of these ionizing spectra does the required amount of oxygen imply that there should be a clearly observable feature for O IV, although for the He II break $\times$ 4 spectrum the expected equivalent width of O IV λ788 is around our 90% confidence limit. This comparison of O V to O IV is virtually independent of our assumptions about the b-parameter and $\sigma_{\rm O}$ since the O V and O IV equivalent widths essentially scale by the same factor for changes in these parameters.

The O IV limit is more interesting for sample I. The predicted equivalent widths are plotted in Figure 16 assuming $\sigma_{\rm O} = 0.5$ dex and $b = 50$ km s^{-1}, which as we argued before is probably more realistic than $b = 10$ km s^{-1} for N(H I)$> 10^{14.2}$ cm^{-2}. Again, the effects of changing the b-parameter and $\sigma_{\rm O}$ are similar to those in Figure 12. For these absorbers, the simulated data suggest that the observed lack of O IV favors a hard ionizing spectrum. For the HM96 spectrum the predicted equivalent width is only slightly higher than our 90% confidence limit. However, for the He II break $\times$ 4 spectrum, the simulations suggest an equivalent width of O IV of more than three times our limit.

This constraint is sensitive to the normalization of the ionizing continuum. An increase in the ionizing flux will decrease $\langle$O IV/O V$\rangle$ resulting in less predicted O IV. We rerun the simulations using $J_\nu = 10^{-21}$ ergs cm^{-2} s^{-1} Hz^{-1} sr^{-1} at 1 Ryd as found by Cooke, Espey, & Carswell (1997). The resulting $\langle$O IV/O V$\rangle$ is smaller by around 30–40%, consistent with the HM96 spectrum but still lying above our upper limit for the softer spectra. Density gradients in the absorbers can also influence the results. By using a constant density, we are assuming that the absorption takes place primarily in the densest portion of the absorber. This should be a good approximation for a given ion provided that the volume density of the ion increases with total density. However, sample I contains absorbers with H I densities near the point where O V peaks. If a significant amount of the absorption were to occur in the density wings of the absorber, the observed $\langle$O IV/O V$\rangle$ would be less than what we have calculated for a constant-density model.

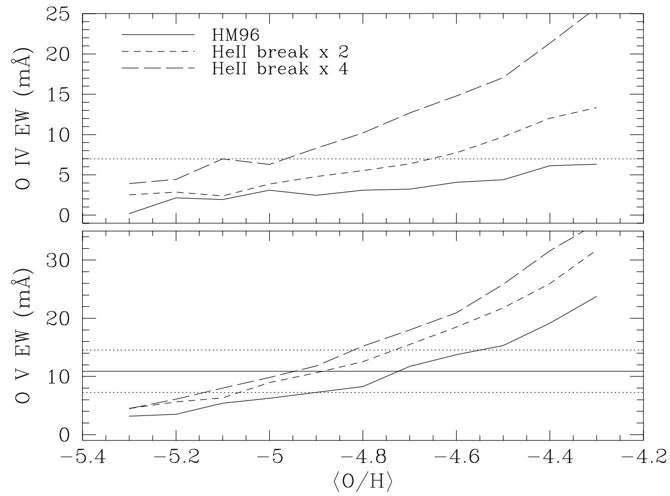

FIG. 15.— Expected equivalent widths of O V λ630 and O IV λ788 as a function of $\langle$O/H$\rangle$ for Lyα absorbers with $10^{13.2} <$ N(H I)$< 10^{14.2}$ cm^{-2}. The different lines correspond to different assumed ionization fractions, as shown in Figure 14, based on different ionizing spectra. For all the simulated data we assume an rms scatter in $\langle$O/H$\rangle$ of 0.5 dex and a b-parameter of 50 km s^{-1}. Our 90% confidence upper limit on the equivalent width of O IV λ788 is shown as the dotted line in the top panel. Our measured value for O V is shown in the bottom panel as it was in Figure 10.

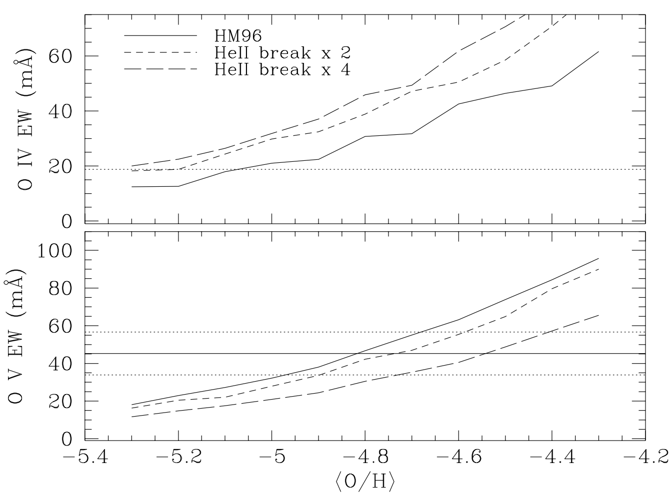

FIG. 16.— Same as Figure 15 for absorbers with N(H I)$> 10^{14.2}$ cm^{-2} and a Lyα equivalent width < 0.6 Å.

An additional consideration is our ignorance of the column densities of the lines in sample I. Because there are only 49 lines in the sample, it is possible that the true distribution of H I column densities is significantly different than our simulated lists. In particular, there could be a relative lack in the true sample of high-column-density systems where $\langle$O IV/O V$\rangle$ is highest. Our simulations suggest that the uncertainty in the predicted O IV equivalent width due to statistical fluctuations in the column-density distribution is comparable to the random noise. The additional uncertainly for O V is much smaller since in our photoionization models N(O V) varies much less with N(H I) over the range of H I column densities spanned by sample I. Models with predicted O IV equivalent widths only moderately above our stated limit are therefore consistent with our results. However, it is quite difficult to reconcile our limit on O IV with the He II break × 4 spectrum. We conclude that our data are probably inconsistent with such a soft ionizing spectrum and that the true ionizing background is not significantly softer than that of HM96.

As we noted above, early observational constraints on $N(\mathrm{He\ II})/N(\mathrm{H\ I})$, often called η, led us to consider ionizing continua softer than HM96. The strongest constraint on η generally considered in the literature is from the He II opacity measurement of Davidsen, Kriss, & Zheng (1996). Recently, Kriss et al. (2001) analyzed a high-resolution spectrum of the He II absorbing region with the Far Ultraviolet Spectroscopic Explorer enabling for the first time the explicit measurement of η for individual absorbers. Using both measured values of η and lower limits for He II absorbers with no corresponding H I absorption, they find a mean η of ~ 80. However, the mean η for absorbers with detectable H I ($N(\mathrm{H\ I}) \gtrsim 10^{12.3}$ cm^{-2}) is ~ 30. Because our sample is selected by H I absorption, it is appropriate to compare to this value. Comparing to the models of Fardal, Giroux, & Shull (1998), $\eta = 30$ suggests a QSO source spectrum with α_{EUV} around -1.6, consistent with Telfer et al. (2002) and similar to HM96. Thus the fact that our data support a hard ionizing continuum is consistent with the He II results if one takes into account that an H I-selected sample preferentially selects absorbers with lower values of η which are likely photoionized by hard, QSO-like radiation.

Including uncertainty in the scatter, our models suggest $\langle \mathrm{O/H} \rangle$ of around -5.2 to -4.6 for sample I, although the required $\langle \mathrm{O/H} \rangle$ could be much higher if the effective b-parameter is much smaller than 50 km s^{-1}. This agrees with the results for sample L, for which the results are more robust due to the fact that the H I column densities of the constituent absorbers are directly measured. We therefore conclude that the typical $\langle \mathrm{O/H} \rangle$ for the IGM likely lies in the range -5.3 to -4.4, as derived for sample L. The abundance with respect to the standard solar value is thus [O/H] around -2.2 to -1.3.

Having derived this abundance, it is interesting to compare this to results from studies of C IV. Using the optical depth ratio technique, Ellison et al. (2000) find that $\langle \mathrm{C\ IV/H\ I} \rangle = -2.6$ for $\tau_{\mathrm{Ly}\alpha} \gtrsim 1$ provides a good match to their data, in agreement with what Songaila & Cowie (1996) found for individually detectable C IV absorbers. Using our HM96 model for the ionization correction for C IV, $\langle \mathrm{C\ IV/H\ I} \rangle = -2.6$ corresponds to $[\mathrm{C/H}] \approx -2.5$. This is in good agreement with what other authors have derived assuming a HM96 spectrum (Hellsten et al. 1997; Davé et al. 1998). The inferred [O/C] is in the range 0.3–1.2, assuming that the chemical composition does not change dramatically from $z \sim 2$ to 3.5 since our results are for slightly lower redshift than those for C IV. Similar results are obtained for the He II break × 2 spectrum. This model implies less carbon, $[\mathrm{C/H}] \approx -2.7$, to match the C IV results, but also less oxygen to match our results, resulting in the same [O/C]. Thus, since the relative ionization corrections in our models for C IV and O V vary little for the H I column densities of interest, the uncertainty in [O/C] is dominated by our uncertainty in $\langle \mathrm{O\ V/H\ I} \rangle$.

An overabundance of oxygen relative to carbon is expected if the IGM is enriched in metals by Type II supernovae. Edvardsson et al. (1993) find overabundances of oxygen relative to carbon by factors of 3–5 in halo stars, consistent with the low end of the range we infer. There is also evidence that this overabundance may increase with decreasing metallicity (Israelian, García López, & Rebolo 1998). A relative overabundance of oxygen is expected from Type II supernova yields (Woosley & Weaver 1995). However, large values of [O/C] may require nucleosynthesis via pair instability supernovae (Heger & Woosley 2002) from very massive stars ($m \gtrsim 100\ M_\odot$) in the early universe (Abia et al. 2001; Schaerer 2002). A bimodal initial mass function for Populations III stars, including a peak at $\sim 100\ M_\odot$, is predicted by the hydrodynamical simulations of Nakamura & Umemura (2001). An additional predicted consequence of nucleosynthesis by very massive stars is a large abundance of silicon, $[\mathrm{Si/C}] \sim 1.0$. In contrast, Songaila & Cowie (1996) infer a typical value of $[\mathrm{Si/C}] \sim 0.4$ for metal-line systems from the observed Si IV / C IV ratios. There is evidence for absorbers with $[\mathrm{Si/C}] \gtrsim 1.0$ at high redshift ($z > 3$), but the assumed implausibility of such abundance ratios are used to argue instead for a substantial softening of the ionizing background (Savaglio et al. 1997; Giroux & Shull 1997; Songaila 1998). Further exploration of the ionizing background at $z > 3$, such as from measurements of the He II / H I and O IV / O V ratios to be made possible by the Cosmic Origins Spectrograph, will help to clarify this issue.

Evidence for an overabundance of oxygen at high redshift has been found by other authors. Reimers et al. (1992) find $[\mathrm{O/C}] \gtrsim 0.6$ for Lyman-limit systems. Using the optical depth technique, Davé et al. (1998) find a good fit for their data using $[\mathrm{O/C}] = 0.5$ for C IV absorbers at $z \gtrsim 3$. However, based on the lack of narrow O VI absorption lines in their data, they claim that the overall metallicity must drop dramatically, by a factor of at least ~ 3, for absorbers with $N(\mathrm{H\ I}) \lesssim 10^{14.5}$ cm^{-2}. In contrast, our results suggest that there is a large abundance of metals at $N(\mathrm{H\ I}) \lesssim 10^{14.2}$ cm^{-2}, consistent with what is found at higher H I column densities. The O VI detection of Schaye et al. (2000) supports this result by suggesting that the enrichment of the IGM does indeed extend to densities below the universal mean.

It is instructive to compare our results to Schaye et al. (2000). Assuming $\langle \mathrm{O\ V/H\ I} \rangle = -1.1$ and using the HM96 model for the ionization correction, for Lyα optical depths ranging from 0.1 to 1.0, corresponding to $10^{13.6} \lesssim N(\mathrm{H\ I}) \lesssim 10^{14.6}$ cm^{-2} for $b = 30$ km s^{-1}, we would predict $\langle \mathrm{O\ VI/H\ I} \rangle$ from around -0.5 for $\tau_{\mathrm{Ly}\alpha} = 0.1$ to -1.3 for $\tau_{\mathrm{Ly}\alpha} = 1.0$. The corresponding ratio of the optical depth of O VI $\lambda 1032$ absorption to Lyα would range from -1.1 to -1.9. This agrees well with the apparent optical depths of O VI measured by Schaye et al. (2000) for the same redshift range, though as they point out, the true optical depth of O VI could be considerably different from the apparent optical depth due to the effects of noise and Lyman-line contamination.

The existence of metals at low column densities addresses the issue of the source of the metals in the IGM. The enrichment of the IGM is thought to occur in one of two basic ways: (1) by a high-redshift era of small star-forming regions, either Population III stars (Ostriker & Gnedin 1996) or protogalaxies (Madau, Ferrara, & Rees 2001), or (2) by in-situ star formation, either in the Lyα absorbers themselves or nearby galaxies. The primary distinction between the two scenarios is the volume extent of the enrichment. While early supernovae could be expected to pre-enrich the universe in a fairly uniform way, it is difficult to enrich the most diffuse regions of the IGM by in-situ star formation. For example, Gnedin & Ostriker (1997) predict a strong dropoff in metallicity at column densities below around $10^{13.5}$–$10^{14.5}$ cm^{-2} at $z = 3$. Although our sample L includes absorbers down to $10^{13.2}$ cm^{-2}, we cannot be sure that there are metals at such low column densities, though the fact that the S/N of the detection does not decrease until we include absorbers with N(H I)$< 10^{13.2}$ cm^{-2} certainly provides evidence that there are metals at low column density. Our results apply to slightly lower redshifts than this prediction, so there is more time for metals to diffuse into less dense regions, and the absorbers that we observe correspond to slightly larger overdensities for the same N(H I). Given these considerations, we cannot conclusively claim that our results are inconsistent with in-situ enrichment scenarios, which are currently an active area of study (Ferrara, Pettini, & Shchekinov 2000; Aguirre et al. 2001). However, it is fair to say that our detection of O V in sample L, in conjuction with previous detections of C IV and O VI in similar density regimes, provide evidence for the presence of metals at quite low column densities, which would favor a uniform enrichment as provided by an early era of star formation.

6. SUMMARY

We have used *HST* FOS spectra of four QSOs to search for absorption features associated with Lyα forest absorbers in the EUV in the redshift range $1.6 < z < 2.9$. The results of this search can be summed up as follows:

1. We detect O V λ630 over a large range of N(H I). Most interestingly, we detect O V in a sample of absorbers with $10^{13.2} < N$(H I)$< 10^{14.2}$ cm^{-2} with greater than 99% confidence.

2. We detect O IV λ788, O IV λ554, O III λ833, and He I λ584 only for the strongest absorbers in our sample, those with Lyα equivalent widths $\gtrsim 0.6$ Å.

3. We find no evidence for N IV λ765, Ne V λ568, Ne VI λ559, Ne VIII $\lambda\lambda$770, 780, or Mg X $\lambda\lambda$610, 625 absorption in any of our samples.

For absorbers with Lyα equivalent widths $\lesssim 0.6$ Å, the O V detections imply $\langle$O V/H I$\rangle \approx -1.7$ to -0.6 based on our simulated data, where this range allows for uncertainties in the assumed b-parameter and scatter in $\langle$O V/H I$\rangle$. This result implies that O V is typically a factor of $\sim 10 - 100$ more abundant than C IV. The O V λ630 line thus has EW/λ a factor of $\sim 30 - 300$ larger than C IV λ1548, or ranging in strength from around that of Lyδ to Lyβ, making it an excellent tracer of metal content.

Using photoionization models to calculate the ionization correction, we find that the oxygen abundance in the IGM is [O/H] ≈ -2.2 to -1.3, implying [O/C] ≈ 0.3 to 1.2, consistent with what is found in halo stars and Lyman-limit systems. The overabundance of oxygen suggests Type II supernova enrichment, but an unusual stellar initial mass function resulting in a significant contribution from pair instability supernovae of very massive ($m \gtrsim 100\ M_\odot$) Population III stars may be necessary.

The fact that we find no evidence for O IV λ788 absorption except in the strongest systems provides an interesting constraint on the ionizing background spectrum, specifically that it is unlikely to be more than a factor of ~ 2 softer than the HM96 spectrum at 4 Ryd. A hard ionizing spectrum is consistent with measurements of He II absorption for absorbers with detectable H I.

We conclude that studying the absorption of the IGM in the rest-frame EUV is not only a useful but essential tool for gaining a more complete understanding of the metal content and ionization of the IGM. From longer wavelength data alone one cannot place useful constraints on absorption from multiple ionization stages of the same element in the diffuse IGM. Ultimately, a more complete understanding requires such analysis, and the clearest path to this end is through the simultaneous study of multiple ionization stages of oxygen (O III–O VI). We look forward to the installment of the Cosmic Origins Spectrograph on the *HST*, currently planned for 2004, which will enormously increase our ability to observe weak oxygen features on an individual basis.

We are grateful to A. Songaila for providing us with the Keck spectrum of HE 2347–4342.

REFERENCES

Abia, C., Domínguez, I., Straniero, O., Limongi, M., Chieffi, A., & Isern, J. 2001, ApJ, 557, 126
Aguirre, A., Hernquist, L., Schaye, J., Katz, N., Weinberg, D. H., & Gardner, J. 2001, ApJ, 561, 521
Barlow, T. A. & Tytler, D. 1998, AJ, 115, 1725
Cooke, A. J., Espey, B., & Carswell, R. F. 1997, MNRAS, 284, 552
Cowie, L. L. & Songaila, A. 1998, Nature, 394, 44
Cowie, L. L., Songaila, A., Kim, T., & Hu, E. M. 1995, AJ, 109, 1522
Croft, R. A. C., Weinberg, D. H., Katz, N., & Hernquist, L. 1997, ApJ, 488, 532
Davé, R., Hellsten, U., Hernquist, L., Katz, N., & Weinberg, D. H. 1998, ApJ, 509, 661
Davidsen, A. F., Kriss, G. A., & Zheng, W. 1996, Nature, 380, 47
de Bernardis, P. et al. 2002, ApJ, 564, 559
de la Varga, A., Reimers, D., Tytler, D., Barlow, T., & Burles, S. 2000, A&A, 363, 69
Edvardsson, B., Andersen, J., Gustafsson, B., Lambert, D. L., Nissen, P. E., & Tomkin, J. 1993, A&A, 275, 101
Ellison, S. L., Lewis, G. F., Pettini, M., Chaffee, F. H., & Irwin, M. J. 1999, ApJ, 520, 456
Ellison, S. L., Songaila, A., Schaye, J., & Pettini, M. 2000, AJ, 120, 1175
Fardal, M. A., Giroux, M. L., & Shull, J. M. 1998, AJ, 115, 2206
Ferland, G. J. 1996, Hazy, a Brief Introduction to Cloudy, Univ. Kentucky, Dept. Physics & Astron. Internal Rep.
Ferrara, A., Pettini, M., & Shchekinov, Y. 2000, MNRAS, 319, 539
Giallongo, E., Cristiani, S., D'Odorico, S., Fontana, A., & Savaglio, S. 1996, ApJ, 466, 46
Giroux, M. L. & Shull, J. M. 1997, AJ, 113, 1505
Gnedin, N. Y. & Ostriker, J. P. 1997, ApJ, 486, 581
Haardt, F. & Madau, P. 1996, ApJ, 461, 20 (HM96)
Hamann, F., Barlow, T. A., & Junkkarinen, V. 1997, ApJ, 478, 87
Heger, A. & Woosley, S. E. 2002, ApJ, 567, 532
Hellsten, U., Davé, R., Hernquist, L., Weinberg, D. H., & Katz, N. 1997, ApJ, 487, 482
Hellsten, U., Hernquist, L., Katz, N., & Weinberg, D. H. 1998, ApJ, 499, 172
Hu, E. M., Kim, T., Cowie, L. L., Songaila, A., & Rauch, M. 1995, AJ, 110, 1526
Hui, L. & Gnedin, N. Y. 1997, MNRAS, 292, 27
Israelian, G., García López, R. J., & Rebolo, R. 1998, ApJ, 507, 805
Jannuzi, B. T. et al. 1996, ApJ, 470, L11
Köhler, S., Reimers, D., Tytler, D., Hagen, H.-J., Barlow, T., & Burles, S. 1999, A&A, 342, 395
Katz, N., Weinberg, D. H., & Hernquist, L. 1996, ApJS, 105, 19
Kim, T., Hu, E. M., Cowie, L. L., & Songaila, A. 1997, AJ, 114, 1

Kirkman, D. & Tytler, D. 1997, ApJ, 484, 672
Kriss, G. A. et al. 2001, Science, 293, 1112
Lu, L. 1991, ApJ, 379, 99
Lu, L., Sargent, W. L. W., Barlow, T. A., Churchill, C. W., & Vogt, S. S. 1996, ApJS, 107, 475
Lu, L. & Savage, B. D. 1993, ApJ, 403, 127
Madau, P., Ferrara, A., & Rees, M. J. 2001, ApJ, 555, 92
Nakamura, F. & Umemura, M. 2001, ApJ, 548, 19
Norris, J., Peterson, B. A., & Hartwick, F. D. A. 1983, ApJ, 273, 450
O'Meara, J. M., Tytler, D., Kirkman, D., Suzuki, N., Prochaska, J. X., Lubin, D., & Wolfe, A. M. 2001, ApJ, 552, 718
Ostriker, J. P. & Gnedin, N. Y. 1996, ApJ, 472, L63
Petitjean, P., Webb, J. K., Rauch, M., Carswell, R. F., & Lanzetta, K. 1993, MNRAS, 262, 499
Pettini, M., Lipman, K., & Hunstead, R. W. 1995, ApJ, 451, 100
Rauch, M., Carswell, R. F., Chaffee, F. H., Foltz, C. B., Webb, J. K., Weymann, R. J., Bechtold, J., & Green, R. F. 1992, ApJ, 390, 387
Rauch, M., Haehnelt, M. G., & Steinmetz, M. 1997, ApJ, 481, 601
Reimers, D. & Vogel, S. 1993, A&A, 276, L13
Reimers, D., Vogel, S., Hagen, H.-J., Engels, D., Groote, D., Wamsteker, W., Clavel, J., & Rosa, M. R. 1992, Nature, 360, 561
Rosa, M. P., Kerber, F., & Keyes, C. D. 1998, Zero-Points of FOS Wavelength Scales (Instrum. Sci. Rep. CAL/FOS-149) (Baltimore: STScI)
Sargent, W. L. W., Young, P. J., Boksenberg, A., & Tytler, D. 1980, ApJS, 42, 41
Savaglio, S., Cristiani, S., D'Odorico, S., Fontana, A., Giallongo, E., & Molaro, P. 1997, A&A, 318, 347
Schaerer, D. 2002, A&A, 382, 28
Schaye, J., Rauch, M., Sargent, W. L. W., & Kim, T. 2000, ApJ, 541, L1
Scott, J., Bechtold, J., Dobrzycki, A., & Kulkarni, V. P. 2000, ApJS, 130, 67
Songaila, A. 1998, AJ, 115, 2184
Songaila, A. & Cowie, L. L. 1996, AJ, 112, 335
Telfer, R. C., Zheng, W., Kriss, G. A., & Davidsen, A. F. 2002, ApJ, 565, 773
Theuns, T., Leonard, A., Efstathiou, G., Pearce, F. R., & Thomas, P. A. 1998, MNRAS, 301, 478
Tytler, D. 1987, ApJ, 321, 49
Tytler, D. & Fan, X. 1994, ApJ, 424, L87
Tytler, D., Fan, X.-M., Burles, S., Cottrell, L., Davis, C., Kirkman, D., & Zuo, L. 1995, in QSO Absorption Lines, ed. G. Meylan (Garching:ESO), 289
Verner, D. A., Tytler, D., & Barthel, P. D. 1994, ApJ, 430, 186
Vogel, S. & Reimers, D. 1993, A&A, 274, L5
—. 1995, A&A, 294, 377
Williger, G. M., Carswell, R. F., Webb, J. K., Boksenberg, A., & Smith, M. G. 1989, MNRAS, 237, 635
Woosley, S. E. & Weaver, T. A. 1995, ApJS, 101, 181
Zhang, Y., Anninos, P., Norman, M. L., & Meiksin, A. 1997, ApJ, 485, 496